
An Energy Stable Approach for Discretizing Hyperbolic Equations with Nonconforming Discontinuous Galerkin Methods

Jeremy E. Kozdon · Lucas C. Wilcox

01 June 2017

Abstract When nonconforming, discontinuous Galerkin methods are implemented for hyperbolic equations using quadrature, exponential energy growth can result even when the underlying scheme with exact integration does not support such growth. Using linear elasticity as a model problem, we propose a skew-symmetric formulation that has the same energy stability properties for both exact and inexact, quadrature-based integration. These stability properties are maintained even when the material properties are variable and discontinuous, and the elements non-affine (e.g., curved). The analytic stability results are confirmed through numerical experiments demonstrating the stability as well as the accuracy of the method.

Keywords discontinuous Galerkin · nonconforming meshes · energy stability · linear elasticity · skew-symmetry

Mathematics Subject Classification (2010) 65M12 · 65M60

1 Introduction

In this paper we consider the energy stability of the (semidiscrete) discontinuous Galerkin method on nonconforming meshes. The two key building blocks for the work are the use of a skew-symmetric form of the governing equations and the projection (or interpolation) of both the trial and test functions to the nonconforming mortar elements.

It has long been recognized that discretizing hyperbolic equations in skew-symmetric form is advantageous; see for instance [25]. Recently, there has been a

J. E. Kozdon: Work partially supported by National Science Foundation Award EAR-1547596 and Office of Naval Research Award N0001416WX01290

J. E. Kozdon · Lucas C. Wilcox
Department of Applied Mathematics, Naval Postgraduate School, Monterey, CA, USA
E-mail: {jekozdon,lwilcox}@nps.edu

resurgence of interest in skew-symmetric formulation in order to improve the robustness of high-order methods; see for instance [11, 22, 8, 16, 18, 20, 10]. From the perspective of discontinuous Galerkin methods, one interpretation of the skew-symmetric form is that it decouples the stability of the equations into a volume and surface component. The stability of the volume terms comes directly from the use of the weak derivative (derivatives of the test functions) and the stability of the surface terms coming from a suitably chosen flux. Key to the skew-symmetric form is that there is no need for a discrete integration-by-parts property (e.g., summation-by-parts [19]) nor a discrete chain rule. We note that when the operators do have a summation-by-parts property this can be used to flip the weak derivatives back to strong derivative without impacting the stability of the method (though in the nonconforming method presented here the surface integrals that results from this procedure would be over an element face and not the corresponding mortar element).

Skew-symmetry also ensures that the same treatment is used for nonconforming faces on the primal and discrete adjoint equations. For example, this can be useful when developing discretely exact discretizations for hyperbolic optimization problems [23].

In this work, we merge the ideas of skew-symmetry with non-conforming meshes. In many ways, the discontinuous Galerkin method is ideal for nonconforming discretizations due the discontinuous nature of the solution space. Kopriva [14] and Kopriva, Woodruff, and Hussaini [17] laid much of the groundwork for the use of nonconforming, discontinuous Galerkin method for hyperbolic problems. These methods were analyzed by Bui-Thanh and Ghattas [3], where it was shown that when inexact quadrature is used, constant coefficient problems on affine meshes can have energy growth that is not present in the method when exact integration is used.

Here we expand upon the literature related to skew-symmetric discretizations by showing that the skew-symmetric approach is of value for nonconforming methods (either due to hanging nodes in the mesh or changes in element spaces). The two critical pieces in this work are:

- The use of a skew-symmetric form for linear elasticity so that integration by parts is not needed discretely
- Evaluation of the skew-symmetric surface integrals in a mortar space so that all surface integrals are consistent even when variational crimes are present

The first point, as noted above, is now well-known in the literature. The second point, is the core contribution of the work and a point which has not been discussed previously in the literature. Unlike many previous skew-symmetric formulations, for nonconforming meshes skew-symmetry is also of value for constant coefficient problems on affine meshes in order to remove potential exponential energy when inexact quadrature is used¹.

Throughout we take variable coefficient, elastodynamics as a model problem, though the approach is straight-forward to generalize to other linear wave problems

¹ Even in the conforming case, some elements (e.g., wedges) and choices of quadrature rules (e.g., SEM quadrature for the quadrilateral face of pyramids) necessitate the use of a skew-symmetric form even for constant coefficient on affine meshes [8].

which can be written in skew-symmetric form. In the results section we consider isoparametric, hexahedral but the stability analysis applies to other element types.

2 Continuous Problem

We consider a velocity-stress formulation of time-dependent linear elasticity in the domain $\Omega \subset \mathbb{R}^d$:

$$\rho \frac{\partial v_i}{\partial t} = \frac{\partial \sigma_{ij}}{\partial x_j}, \quad \frac{\partial \sigma_{ij}}{\partial t} = \frac{1}{2} C_{ijkl} \left(\frac{\partial v_i}{\partial x_j} + \frac{\partial v_j}{\partial x_i} \right), \quad (1)$$

where $d = 2$ or $d = 3$. Unless otherwise noted, summation over 1, 2, 3 is implied for terms with twice repeated subscripts; free subscripts can take any of the values 1, 2, 3; and in the case of $d = 2$ the derivatives with respect to x_3 are taken to be 0. Here v_i is the particle velocity in the x_i direction and σ_{ij} are the components of the symmetric stress tensor such that $\sigma_{ij} = \sigma_{ji}$. The scalar ρ is the density of the material and C_{ijkl} are the components of the fourth order stiffness tensor which has the symmetries: $C_{ijkl} = C_{klij} = C_{jikl} = C_{ijlk}$. In the results, §5, isotropic elasticity is considered where

$$C_{ijkl} = \lambda \delta_{ij} \delta_{kl} + \mu (\delta_{ik} \delta_{jl} + \delta_{il} \delta_{jk}), \quad (2)$$

with λ and μ denoting Lamé's first and second parameters (μ is also known as the shear modulus), and δ_{ij} denoting the Kronecker delta which takes a value of 1 if $i = j$ and 0 otherwise. Both ρ and C_{ijkl} are allowed to be spatially dependent and may include jump discontinuities.

Since the focus of this work is the treatment of non-conforming mesh interfaces, only the traction free boundary condition on $\partial\Omega$ is considered. That is, if n_i is a component of the outward pointing normal vector to $\partial\Omega$ and $T_i = \sigma_{ij} n_j$ are components of the traction vector, then the boundary condition is $T_i = 0$ on $\partial\Omega$.

Critical to the stability analysis that follows is the existence of an energy norm in which the energy of the semi-discrete numerical scheme is non-increasing. This is motivated by the fact that the continuous problem with the traction free boundary condition does not support energy growth, where the energy in the solution is defined as

$$\mathcal{E} = \int_{\Omega} \left(\frac{\rho}{2} v_i v_i + \frac{1}{2} \sigma_{ij} S_{ijkl} \sigma_{kl} \right). \quad (3)$$

Here S_{ijkl} denotes the components of the fourth order compliance tensor which is the inverse of the stiffness tensor, i.e., $s_{ij} C_{ijkl} S_{klmn} s_{nm} = s_{ij} s_{ij}$ for all symmetric second order tensors with components s_{ij} . The energy equation (3) is a well-defined norm if $\rho > 0$ and the compliance tensor is positive definite, i.e., $s_{ij} S_{ijkl} s_{kl} > 0$ for all non-zero, symmetric second order tensors with components s_{ij} (e.g., see [21]). In the case of isotropic elasticity the components of the compliance tensor are

$$S_{ijkl} = -\frac{\lambda}{2\mu(2\mu + 3\lambda)} \delta_{ij} \delta_{kl} + \frac{1}{4\mu} (\delta_{ik} \delta_{jl} + \delta_{il} \delta_{jk}), \quad (4)$$

and the compliance tensor is positive definite if $\mu > 0$ and $K = \lambda + 2\mu/3 > 0$; K is known as the bulk modulus of the material.

To see that the traction free boundary condition does not lead to energy growth, the time derivative of the energy equation (3) is considered:

$$\frac{d\mathcal{E}}{dt} = \int_{\Omega} \left(\rho v_i \frac{\partial v_i}{\partial t} + \sigma_{ij} S_{ijkl} \frac{\partial \sigma_{kl}}{\partial t} \right) = \int_{\Omega} \left(v_i \frac{\partial \sigma_{ij}}{\partial x_j} + \sigma_{ij} \frac{\partial v_i}{\partial x_j} \right) \quad (5)$$

where (1) has been used to change time derivatives into spatial derivatives. By applying the divergence theorem and substituting in the traction free boundary condition, the energy rate of change is then

$$\frac{d\mathcal{E}}{dt} = \int_{\partial\Omega} v_i \sigma_{ij} n_j = \int_{\partial\Omega} v_i T_i = 0. \quad (6)$$

We formalize this in the following theorem.

Theorem 1 *Problem (1) with the traction free boundary condition $T_i = 0$ on $\partial\Omega$ satisfies the energy estimate $\mathcal{E}(t) = \mathcal{E}(0)$.*

Proof Integrating (6) gives the result $\mathcal{E}(t) = \mathcal{E}(0)$. \square

3 Notation for the Discontinuous Galerkin Method

3.1 Mesh and Geometry Transformation

In this work, the finite element mesh is thought of as being defined in two steps. First, the domain is partitioned into a set of non-overlapping elements the union of which completely covers the domain. It is assumed that there is an exact transformation between these physical elements and a set of reference elements. After this, approximation errors are allowed for in the mappings between the physical and reference elements which may result in gaps and overlaps in the mesh and a set of elements whose union is no longer equal to the domain. This could arise if, for instance, one used an isoparametric approximation for the geometry on a nonconforming mesh; other approximations for the geometry are possible as long as the introduced quadrature rules satisfy the constraints given in §3.3.

Initially we let Ω be partitioned into a finite set of non-overlapping, possibly nonconforming, d -dimensional, curved volume elements. Let \mathbb{E} denote the set of all elements and $|\mathbb{E}|$ be the total number of volume elements. At this initial stage, we require that $\bigcup_{e \in \mathbb{E}} e = \Omega$. These requirements on the partitioning of Ω imply that before approximation errors are introduced the mesh has no gaps. In the computational results, §5, $d = 3$ is considered with curvilinear hexahedral elements, though the stability analysis is more general.

Let $\Gamma = \bigcup_{e \in \mathbb{E}} \partial e$ where ∂e is the boundary of element e ; we call Γ the mortar and it contains both the internal mesh interfaces and the outer boundary. The mortar is partitioned into a (finite) set of non-overlapping, $(d-1)$ -dimensional mortar elements; the set of mortar elements is denoted by \mathbb{M} . The number of mortar

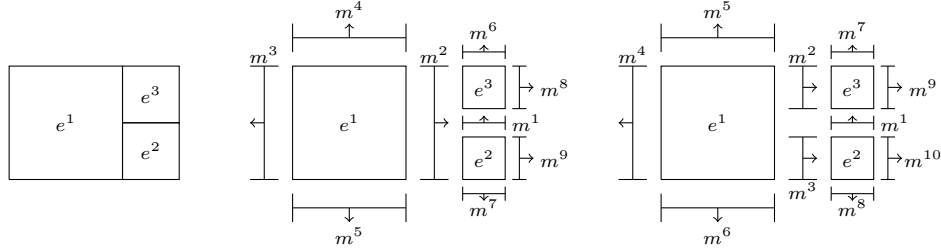


Fig. 1 (left) Example of a nonconforming mesh. (center) Example of a mortar decomposition of the mesh, where the mortar elements are conforming to the larger element across the nonconforming faces. (right) Example of a mortar decomposition of the mesh, where the mortar elements conform to the smaller elements across the nonconforming faces. (center and right) The arrows on the mortar faces represent the direction of the canonical (and arbitrary) mortar element normals. In both the center and right figures, the mortar elements on the boundary of the domain are not shown.

elements is $|\mathbb{M}|$ and we require that $\bigcup_{m \in \mathbb{M}} m = \Gamma$. Fig. 1 contains an example volume mesh and two possible mortar meshes. The center and right panel shows two different partitioning of the (internal) mortar for the volume mesh in the left panel.

The set \mathbb{M}^e is defined to be the set of mortar elements that volume element $e \in \mathbb{E}$ connects to, namely

$$\mathbb{M}^e = \{m \in \mathbb{M}^e | m \in \mathbb{M} \text{ and } m \cap \partial e \neq \emptyset\}. \quad (7)$$

Similarly the set \mathbb{E}^m is defined to be the set of volume element that mortar element $m \in \mathbb{M}$ connects to:

$$\mathbb{E}^m = \{e \in \mathbb{E}^m | e \in \mathbb{E} \text{ and } m \cap \partial e \neq \emptyset\}. \quad (8)$$

It is useful to further partition \mathbb{E}^m into two subsets depending on which side of the mortar each element resides. To do this, each mortar element $m \in \mathbb{M}$ is given a canonical orientation defined by a unit normal (the orientation of which is arbitrary); the components of the unit normal for m are denoted n_i^m . If a volume elements $e \in \mathbb{E}^m$ is on the side of the mortar towards which the normal points the element is said to be on the *plus-side* of the mortar, otherwise it is said to be on the *minus-side* of the mortar. The set of volume elements on the plus and minus side of mortar element $m \in \mathbb{E}^m$ are denoted by \mathbb{E}^{+m} and \mathbb{E}^{-m} , respectively, and $\mathbb{E}^m = \mathbb{E}^{+m} \cup \mathbb{E}^{-m}$. For the example mesh shown in the center panel of Fig. 1 the above defined sets are:

$$\begin{aligned} \mathbb{M}^{e^1} &= \{m^2, m^3, m^4, m^5\}, & \mathbb{E}^{m^1} &= \{e^1, e^2, e^3\}, & \mathbb{E}^{m^2} &= \{e^2, e^3\}, \\ \mathbb{M}^{e^2} &= \{m^1, m^2, m^7, m^9\}, & \mathbb{E}^{+m^1} &= \{e^2, e^3\}, & \mathbb{E}^{+m^2} &= \{e^3\}, \\ \mathbb{M}^{e^3} &= \{m^1, m^2, m^6, m^8\}, & \mathbb{E}^{-m^1} &= \{e^1\}, & \mathbb{E}^{-m^2} &= \{e^1\}. \end{aligned} \quad (9)$$

Each element $e \in \mathbb{E}$ is taken to have a reference element \hat{e} where the discretization is specified. It is assume that there exists a diffeomorphic mapping between the

reference and physical element. That is, there exists differentiable functions \mathbf{x}^e and \mathbf{r}^e such that if $\mathbf{r} \in \hat{e}$ then $\mathbf{x}^e(\mathbf{r}) \in e$ and if $\mathbf{x} \in e$ then $\mathbf{r}^e(\mathbf{x}) \in \hat{e}$. Similarly, for each mortar element $m \in \mathbb{M}$ it is assumed that there exists a reference mortar element \hat{m} along with the transforms \mathbf{x}^m and \mathbf{r}^m .

For the exact transformation, the Jacobian determinant for volume element $e \in \mathbb{E}$ is denoted J^e . For $d = 2$ the Jacobian determinant is

$$J^e = \frac{\partial x_1^e}{\partial r_1} \frac{\partial x_2^e}{\partial r_2} - \frac{\partial x_1^e}{\partial r_2} \frac{\partial x_2^e}{\partial r_1}, \quad (10)$$

and for $d = 3$

$$J^e = \varepsilon_{ijk} \frac{\partial x_1^e}{\partial r_i} \frac{\partial x_2^e}{\partial r_j} \frac{\partial x_3^e}{\partial r_k}, \quad (11)$$

with ε_{ijk} being the Levi-Civita permutation symbol

$$\varepsilon_{ijk} = \begin{cases} +1, & \text{if } ijk \text{ is } 123, 312, \text{ or } 231, \\ -1, & \text{if } ijk \text{ is } 321, 132, \text{ or } 213, \\ 0, & \text{otherwise.} \end{cases} \quad (12)$$

Similarly, the surface Jacobian for mortar element $m \in \mathbb{M}$ is S_J^m . For $d = 2$, the surface Jacobian for a mortar element is

$$S_J^m = \sqrt{\left(\frac{dx_1^m}{d\xi}\right)^2 + \left(\frac{dx_2^m}{d\xi}\right)^2}, \quad (13)$$

where the parametric curves $(r_1^m(\xi), r_2^m(\xi))$ parameterizes the mortar element and

$$\frac{dx_j^m}{d\xi} = \frac{\partial x_j^m}{\partial r_1} \frac{dr_1^m}{d\xi} + \frac{\partial x_j^m}{\partial r_2} \frac{dr_2^m}{d\xi}. \quad (14)$$

For $d = 3$, the surface Jacobian of a mortar element is

$$S_J^m = \sqrt{\left(\varepsilon_{ijk} \frac{\partial x_j^m}{\partial \xi} \frac{\partial x_k^m}{\partial \eta}\right)^2}, \quad (15)$$

with the mortar element parameterized as $(r_1^m(\xi, \eta), r_2^m(\xi, \eta), r_3^m(\xi, \eta))$ and

$$\frac{\partial x_k^m}{\partial \xi} = \frac{\partial x_k^m}{\partial r_i} \frac{\partial r_i^m}{\partial \xi}, \quad \frac{\partial x_k^m}{\partial \eta} = \frac{\partial x_k^m}{\partial r_i} \frac{\partial r_i^m}{\partial \eta}. \quad (16)$$

3.2 Function Spaces

The finite dimensional approximation space for $e \in \mathbb{E}$ is defined on the reference element \hat{e} , and is denoted by $\hat{V}^e \subset L^2(\hat{e})$ and with dimension $\dim \hat{V}^e$. For the numerical results §5, tensor product polynomials of degree at most N are used:

$$\hat{Q}^{N,d} := \left\{ \prod_{i=1}^d r_i^{n_i} \mid 0 \leq n_i \leq N, \forall i \in [1, d] \right\}. \quad (17)$$

A corresponding space V^e for the physical element can be defined the space of all functions q^e such that $q^e(\mathbf{x}) = q^e(\mathbf{r}^e(\mathbf{x}))$ for some $q^e \in \hat{V}^e$. Similar definitions are used for each mortar element $m \in \mathbb{M}$, with $\hat{U}^m \subset L^2(\hat{m})$ being the finite dimensional space defined on the reference element \hat{m} with dimension $\dim \hat{U}^m$; in the results $\hat{U}^m = \hat{Q}^{N,d-1}$ where N is the same as in the volume approximation.

The operator $\mathcal{P}^{m,e} : \hat{V}^e \rightarrow \hat{U}^m$ is taken to be a linear projection or interpolation operator from volume element $e \in \mathbb{E}$ to mortar element $m \in \mathbb{M}$. It is assumed to have the property that if $q^e \in \hat{V}^e$ then $\mathcal{P}^{m,e} q^e \in \hat{U}^m$. In §5 these are constructed from either L^2 -projections or interpolations depending on the type of mortar element used. For instance, if the mortar elements between non-conforming elements were as shown in the center panel of Fig. 1, then \mathcal{P}^{m_2,e_2} and \mathcal{P}^{m_2,e_3} would be components of the L^2 -projection operator between from e_2 and e_3 to m_2 , and \mathcal{P}^{m_2,e_1} would be an interpolation operator; the construction of \mathcal{P}^{m_2,e_2} and \mathcal{P}^{m_2,e_3} is given in Appendix A. On the other hand, if the mortar elements between non-conforming elements were as shown in the right panel of Fig. 1, then \mathcal{P}^{m_2,e_1} , \mathcal{P}^{m_2,e_3} , \mathcal{P}^{m_3,e_1} , and \mathcal{P}^{m_3,e_2} would all be interpolation operators (assuming that the order of functions on the mortar was greater than or equal to the volume element faces).

If $\zeta_n^e \in \hat{V}^e$ for $n = 1, 2, \dots, \dim \hat{V}^e$ are linearly independent basis functions for \hat{V}^e , then $q^e \in \hat{V}^e$ can be written as

$$q^e = \sum_{n=1}^{\dim \hat{V}^e} q_n^e \zeta_n^e, \quad (18)$$

where q_n^e are the scalar degree of freedom and are stored as the vector

$$\mathbf{q}^e = \begin{bmatrix} q_1^e \\ q_2^e \\ \vdots \\ q_{\dim \hat{V}^e}^e \end{bmatrix}. \quad (19)$$

Similar notation is used to represent functions on the reference mortar element \hat{m} with the vector \mathbf{q}^m being the $\dim \hat{U}^m$ degrees of freedom representing $q^m \in \hat{U}^m$.

3.3 Quadrature

In order to allow for a more general formulation, we allow the exact geometry transformations to be approximated, such as by an isoparametric geometry approximation, which leads to the definition of *approximate* physical elements. Namely, it is

assumed that there exists approximate transformations \mathbf{r}_h^e and \mathbf{x}_h^e which transform between the reference element \hat{e} and an approximate physical element $e_h = \mathbf{r}_h^e(\hat{e})$ where $e_h \approx e$; approximation of the mortar element transforms leads to approximate mortar elements $m_h = r_h^e(\hat{m}) \approx m$. The introduction of the approximate physical elements e_h means that it is possible that $\bigcup_{e_h \in \mathbb{E}_h} e_h = \Omega_h \neq \Omega$. Similarly, depending on how the approximate transformations are defined, the mesh computational mesh may now have gaps between and overlap between neighboring elements.²

The κ^e -weighted inner product over $e \in \mathbb{E}$ between $p^e \in \hat{V}^e$ and $q^e \in \hat{V}^e$ is approximated as

$$\int_{\hat{e}} \kappa^e J^e p^e q^e \approx (\mathbf{p}^e)^T \mathbf{M}_\kappa^e \mathbf{q}^e, \quad (20)$$

where \mathbf{M}_κ^e is a symmetric matrix. If $\kappa^e > 0$ then it is assumed that \mathbf{M}_κ^e is positive definite. This positive definite assumption on the mass matrix \mathbf{M}_κ^e does not require any particularly assumptions concerning the approximation of the geometry transformation, for example the Jacobian determinant could be computed using the exact transformation (11) or computed to respect the metric identities [13].

If S_{ijkl} is a component of a positive definite, fourth order tensor then it is not required that $\mathbf{M}_{S_{ijkl}}^e$ be positive definite (since any individual component of a positive definite tensor need not be positive). That said, it is required that $(\mathbf{s}^e)_{ij}^T \mathbf{M}_{S_{ijkl}}^e \mathbf{s}_{kl}^e \geq 0$ for all symmetric second order tensors whose components $s_{ij}^e \in \hat{V}^e$ satisfy $s_{ij}^e = s_{ji}^e$. Defining

$$\bar{\mathbf{M}}_S^e = \begin{bmatrix} \mathbf{M}_{S_{1111}}^e & \mathbf{M}_{S_{1122}}^e & \mathbf{M}_{S_{1133}}^e & 2\mathbf{M}_{S_{1123}}^e & 2\mathbf{M}_{S_{1113}}^e & 2\mathbf{M}_{S_{1112}}^e \\ \mathbf{M}_{S_{1122}}^e & \mathbf{M}_{S_{2222}}^e & \mathbf{M}_{S_{2233}}^e & 2\mathbf{M}_{S_{2223}}^e & 2\mathbf{M}_{S_{2213}}^e & 2\mathbf{M}_{S_{2212}}^e \\ \mathbf{M}_{S_{1133}}^e & \mathbf{M}_{S_{2233}}^e & \mathbf{M}_{S_{3333}}^e & 2\mathbf{M}_{S_{3323}}^e & 2\mathbf{M}_{S_{3313}}^e & 2\mathbf{M}_{S_{3312}}^e \\ 2\mathbf{M}_{S_{1123}}^e & 2\mathbf{M}_{S_{2223}}^e & 2\mathbf{M}_{S_{3323}}^e & 4\mathbf{M}_{S_{2323}}^e & 4\mathbf{M}_{S_{2313}}^e & 4\mathbf{M}_{S_{2312}}^e \\ 2\mathbf{M}_{S_{1113}}^e & 2\mathbf{M}_{S_{2213}}^e & 2\mathbf{M}_{S_{3313}}^e & 4\mathbf{M}_{S_{2313}}^e & 4\mathbf{M}_{S_{1313}}^e & 4\mathbf{M}_{S_{1312}}^e \\ 2\mathbf{M}_{S_{1112}}^e & 2\mathbf{M}_{S_{2212}}^e & 2\mathbf{M}_{S_{3312}}^e & 4\mathbf{M}_{S_{2312}}^e & 4\mathbf{M}_{S_{1312}}^e & 4\mathbf{M}_{S_{1212}}^e \end{bmatrix}, \quad (21)$$

the above restriction on $\mathbf{M}_{S_{ijkl}}^e$ can be restated as requiring that $\bar{\mathbf{M}}_S^e$ be symmetric, positive definite.

Integrals involving spatial derivatives of the solution are approximated as

$$\int_{\hat{e}} J^e p^e \frac{\partial q^e}{\partial x_j} = \int_{\hat{e}} J^e p^e \frac{\partial r_k^e}{\partial x_j} \frac{\partial q^e}{\partial r_k} \approx (\mathbf{p}^e)^T \mathbf{S}_j^e \mathbf{q}^e, \quad (22)$$

where we highlight the fact that stiffness matrix \mathbf{S}_j^e contains the metric terms. One feature of our discretization is that no summation-by-parts [19] property between stiffness and mass matrices is required.

Surface integrals over $m \in \mathbb{M}$ are assumed to be approximated using a primitive, positive weight, n_q^m -point quadrature rule defined for the reference element \hat{m} . Thus, if $\omega_n^m > 0$ are the weights and \mathbf{r}_n^m are the nodes of the rule (with $n = 1, 2, \dots, n_q^m$)

² In principle one could introduce approximations of the reference elements as well so that $\hat{e} \neq \hat{e}_h$, but since many methods are specified using straight-sided reference elements this is not considered here.

then \mathbf{W}^m is the diagonal matrix of quadrature weights and surface Jacobians evaluated at the quadrature nodes. Namely, the diagonal elements of the matrix are

$$\mathbf{W}_{nn}^m = \omega_n^m S_J^m(\mathbf{r}_n^m) \quad (\text{no summation over } n). \quad (23)$$

If \mathbf{L}^m is interpolation matrix which goes from the degrees of freedom of \hat{U}^m to values at the quadrature nodes, then inner products over the mortar $m \in \mathbb{M}$ between $p^m \in \hat{U}^m$ and $q^m \in \hat{U}^m$ are approximated as

$$\int_{\hat{m}} S_J^m p^m q^m \approx (\mathbf{p}^m)^T (\mathbf{L}^m)^T \mathbf{W}^m \mathbf{L}^m \mathbf{q}^m. \quad (24)$$

If the intersection of the boundary of volume element $e \in \mathbb{E}$ and $m \in \mathbb{M}$ is non-zero, that is $\partial e \cap m \neq \emptyset$, then integrals between $p^m \in \hat{U}^m$ and $q^e \in \hat{V}^e$ are approximated as

$$\int_{\hat{m}} S_J^m p^m \mathcal{P}^{m,e} q^e \approx (\mathbf{p}^m)^T (\mathbf{L}^m)^T \mathbf{W}^m \mathbf{P}^{m,e} \mathbf{q}^e, \quad (25)$$

where we note that $\mathbf{P}^{m,e}$ goes directly from the volume element to the quadrature nodes, and thus includes both the projection operator $\mathcal{P}^{m,e}$ (or its approximation) and the interpolation matrix \mathbf{L}^m .

4 Discontinuous Galerkin Method

4.1 Exact Integration

A skew symmetric, discontinuous Galerkin formulation based on (1) is: For each $e \in \mathbb{E}$, find $v_j^e \in \hat{V}^e$ and symmetric $\sigma_{ij}^e = \sigma_{ji}^e \in \hat{V}^e$ such that for all $\phi_j^e \in \hat{V}^e$ and $\psi_{ij}^e \in \hat{V}^e$ such that $\psi_{ij}^e = \psi_{ji}^e$ the following holds:

$$\int_{\hat{e}} J^e \rho^e \phi_i^e \frac{\partial v_i^e}{\partial t} = - \int_{\hat{e}} J^e \frac{\partial \phi_i^e}{\partial x_j} \sigma_{ij}^e + \sum_{m \in \mathbb{M}^e} \int_{\hat{m}} S_J^m \phi_i^{m,e} T_i^{*m,e}, \quad (26)$$

$$\begin{aligned} \int_{\hat{e}} J^e \psi_{ij}^e S_{ijkl}^e \frac{\partial \sigma_{kl}^e}{\partial t} &= \int_{\hat{e}} \frac{J^e}{2} \psi_{ij}^e \left(\frac{\partial v_i^e}{\partial x_j} + \frac{\partial v_j^e}{\partial x_i} \right) \\ &+ \sum_{m \in \mathbb{M}^e} \int_{\hat{m}} S_J^m (n_j \psi_{ij})^{m,e} (v_i^{*m} - v_i^{m,e}), \end{aligned} \quad (27)$$

with the mortar projected values defined as $v_i^{m,e} = \mathcal{P}^{m,e} v_i^e$ and $\phi_i^{m,e} = \mathcal{P}^{m,e} \phi_i$. The quantity $(n_j \psi_{ij})^{m,e}$ is the *test* traction defined on the mortar. One way to define this quantity is to compute the traction on the element face then project it to the mortar: $(n_j \psi_{ij})^{m,e} = \mathcal{P}^{m,e} n_j^e \psi_{ij}$ where n_j^e is the outward normal for element e . An alternative approach is to project the stress tensor to the mortar and then compute the traction on the mortar: $(n_j \psi_{ij})^{m,e} = n_j^{m,e} \mathcal{P}^{m,e} \psi_{ij}$ where $n_j^{m,e}$ is the mortar normal which is oriented outward to element e . Both approaches will result in a stable numerical method, and in the results section the later approach is used (projecting the stresses). The vectors $T_i^{*m,e}$ and v_i^{*m} are the numerical

fluxes which enforce continuity of traction and velocity across the mortar elements and the physical boundary conditions. The choice of the numerical flux is critical for ensuring the consistency and stability of the method (as discussed below). The superscript e in $T_i^{*m,e}$ denotes the fact that this traction is defined with respect the normal of element e . Namely, if elements e^1 and e^2 are both connected to mortar m then $T_i^{*m,e^1} = T_i^{*m,e^2}$ if both elements are on the same side of the mortar element and $T_i^{*m,e^1} = -T_i^{*m,e^2}$ if they are on opposite sides due to the equal but opposite normal vector.

An important feature of (26)–(27) is that the surface integrals are evaluated on the mortar elements, not the volume element faces. This structure essentially decouples the volume and surface stability, leading to a semi-discretely stable scheme even when quadrature (or under-integration) is used.

The energy in element e is defined as

$$\mathcal{E}^e = \int_{\hat{e}} J^e \left(\frac{\rho}{2} v_i^e v_i^e + \frac{1}{2} \sigma_{ij}^e S_{ijkl}^e \sigma_{kl}^e \right), \quad (28)$$

with $\mathcal{E} = \sum_{e \in \mathbb{E}} \mathcal{E}_e$ being the energy in the entire domain; see (3). Since the continuous problem does not support energy growth, it is desirable that the semi-discrete problem mimic this property, e.g., $d\mathcal{E}/dt \leq 0$. For each element, the energy rate of change is

$$\frac{d\mathcal{E}^e}{dt} = \sum_{m \in \mathbb{M}^e} \frac{d\mathcal{E}^{m,e}}{dt}, \quad (29)$$

$$\frac{d\mathcal{E}^{m,e}}{dt} = \int_{\hat{m}} S_J^m \left(v_i^{m,e} T_i^{-*m} + v_i^{*m} T_i^{m,e} - v_i^{m,e} T_i^{m,e} \right), \quad (30)$$

where $d\mathcal{E}^{m,e}/dt$ is the contribution to the energy rate of change for mortar element $m \in \mathbb{M}^e$ that comes from element $e \in \mathbb{E}^m$. Here the traction vector $T_i^{m,e} = (n_j \sigma_{ij})^{m,e}$, is either the projection of the tractions to the mortar or the tractions defined from the projected stresses; see discussion following (27).

In order to complete the energy estimate, a single mortar element $m \in \mathbb{M}$ is considered and the contribution from all elements that overlap with this mortar element are added together:

$$\frac{d\mathcal{E}^m}{dt} = \sum_{e \in \mathbb{E}^m} \frac{d\mathcal{E}^{m,e}}{dt}. \quad (31)$$

By defining the mortar plus and minus states

$$v_i^{\pm m} = \sum_{e \in \mathbb{E}^{\pm m}} v_i^{m,e}, \quad T_i^{\pm m} = \mp \sum_{e \in \mathbb{E}^{\pm m}} T_i^{m,e}, \quad (32)$$

the mortar element energy rate of change can be written as

$$\begin{aligned} \frac{d\mathcal{E}^m}{dt} = \int_{\hat{m}} S_J^m \left((v_i^{-m} - v_i^{+m}) T_i^{*m} + v_i^{*m} (T_i^{-m} - T_i^{+m}) \right. \\ \left. - v_i^{-m} T_i^{-m} + v_i^{+m} T_i^{+m} \right). \end{aligned} \quad (33)$$

Here, the velocity components of the numerical flux are $v_i^{*m} = v_i^{*m,e}$ for all $e \in \mathbb{E}^m$ and the traction component of the numerical flux $T_i^{*m} = T^{*m,e}$ if $e \in \mathbb{E}^{-m}$ and $T_i^{*m} = -T^{*m,e}$ if $e \in \mathbb{E}^{+m}$. For mortar elements on the physical boundary, the energy rate of change is

$$\frac{d\mathcal{E}^m}{dt} = \int_{\hat{m}} S_J^m \left(v_i^{-m} T_i^{*m} + v_i^{*m} T_i^{-m} - v_i^{-m} T_i^{-m} \right). \quad (34)$$

If the numerical flux is defined such that the integrand of (33) and (34) are non-positive for all $v_i^{\pm m}$ and $T_i^{\pm m}$, then the following theorem results.

Theorem 2 *If there exists a numerical flux such that the integrand of the energy rate (33) and (34) are non-positive, then discontinuous Galerkin method (26)–(27) satisfies the energy estimate $\mathcal{E}(t) \leq \mathcal{E}(0)$ and is energy stable.*

Proof Taking the derivative of the energy gives,

$$\frac{d\mathcal{E}}{dt} = \sum_{e \in \mathbb{E}} \frac{d\mathcal{E}^e}{dt} = \sum_{m \in \mathbb{M}} \frac{d\mathcal{E}^m}{dt}. \quad (35)$$

If across every face the numerical fluxes have the property that (33) and (34) are non-positive it follows that

$$\frac{d\mathcal{E}}{dt} \leq 0, \quad (36)$$

and $\mathcal{E}(t) \leq \mathcal{E}(0)$ results upon integration. \square

4.2 Definition of the numerical flux for isotropic elasticity.

Of course, the critical question then becomes: can numerical fluxes be defined so that (33) and (34) are non-positive. For isotropic elasticity, one approach is to use a flux defined as

$$T_i^{*m} = n_i^m T_{\parallel}^{*m} + T_{i\perp}^{*m}, \quad v_i^{*m} = n_i^m v_{\parallel}^{*m} + v_{i\perp}^{*m}, \quad (37)$$

where T_{\parallel}^{*m} and v_{\parallel}^{*m} are the mortar parallel traction and velocity, and $T_{i\perp}^{*m}$ and $v_{i\perp}^{*m}$ the mortar perpendicular components. To define these terms, it is necessary to first define the parallel and perpendicular plus and minus states:

$$T_{\parallel}^{\pm m} = n_i T_i^{\pm m}, \quad T_{i\perp}^{\pm m} = T_i^{\pm m} - n_i T_{\parallel}^{\pm m}, \quad (38)$$

$$v_{\parallel}^{\pm m} = n_i v_i^{\pm m}, \quad v_{i\perp}^{\pm m} = v_i^{\pm m} - n_i v_{\parallel}^{\pm m}. \quad (39)$$

With this, the terms in flux (37) can be defined as

$$T_{\parallel}^{*m} = k_p^m \left(Z_p^{+m} T_{\parallel}^{-m} + Z_p^{-m} T_{\parallel}^{+m} - \alpha Z_p^{-m} Z_p^{+m} \left(v_{\parallel}^{-m} - v_{\parallel}^{+m} \right) \right) \quad (40)$$

$$v_{\parallel}^{*m} = k_p^m \left(Z_p^{-m} v_{\parallel}^{-m} + Z_p^{+m} v_{\parallel}^{+m} - \alpha \left(T_{\parallel}^{-m} - T_{\parallel}^{+m} \right) \right), \quad (41)$$

$$T_{i\perp}^{*m} = k_s^m \left(Z_s^{+m} T_{i\perp}^{-m} + Z_s^{-m} T_{i\perp}^{+m} - \alpha Z_s^{-m} Z_s^{+m} \left(v_{i\perp}^{-m} - v_{i\perp}^{+m} \right) \right), \quad (42)$$

$$v_{i\perp}^{*m} = k_s^m \left(Z_s^{-m} v_{i\perp}^{-m} + Z_s^{+m} v_{i\perp}^{+m} - \alpha \left(T_{i\perp}^{-m} - T_{i\perp}^{+m} \right) \right), \quad (43)$$

with the material properties entering the flux definition through the following relationships

$$Z_s^{\pm m} = \sqrt{\rho^{\pm m} \mu^{\pm m}}, \quad Z_p^{\pm m} = \sqrt{\rho^{\pm m} (\lambda^{\pm m} + 2\mu^{\pm m})}, \quad (44)$$

$$k_s^m = \frac{1}{Z_s^{-m} + Z_s^{+m}}, \quad k_p^m = \frac{1}{Z_p^{-m} + Z_p^{+m}}. \quad (45)$$

Here the parameter $\alpha \geq 0$ controls the amount of dissipation that occurs through the flux, with $\alpha = 1$ being the upwind flux [24] and $\alpha = 0$ being a central-like flux which results in no-energy dissipation across the interface. To enforce the physical boundary condition $T_i = 0$ we set $v_i^{+m} = v_i^{-m}$, $T_i^{+m} = -T_i^{-m}$, $Z_s^{+m} = Z_s^{-m}$, and $Z_p^{+m} = Z_p^{-m}$ which leads to

$$T_{\parallel}^{*m} = 0, \quad v_{\parallel}^{*m} = v_{\parallel}^{-m} - \alpha \frac{T_{\parallel}^{-m}}{Z_p^{-m}}, \quad T_{i\perp}^{*m} = 0, \quad v_{i\perp}^{*m} = v_{i\perp}^{-m} - \alpha \frac{T_{i\perp}^{-m}}{Z_s^{-m}}. \quad (46)$$

To see that (37) results in a stable flux, first consider the interior mortar rate of energy change integral (33). Rewriting the integrand in terms of the parallel and perpendicular components gives

$$\begin{aligned} & (v_i^{-m} - v_i^{+m}) T_i^{*m} + v_i^{*m} (T_i^{-m} - T_i^{+m}) - v_i^{-m} T_i^{-m} + v_i^{+m} T_i^{+m} \\ &= (v_{\parallel}^{-m} - v_{\parallel}^{+m}) T_{\parallel}^{*m} + v_{\parallel}^{*m} (T_{\parallel}^{-m} - T_{\parallel}^{+m}) - v_{\parallel}^{-m} T_{\parallel}^{-m} + v_{\parallel}^{+m} T_{\parallel}^{+m} \\ &+ (v_{i\perp}^{-m} - v_{i\perp}^{+m}) T_{i\perp}^{*m} + v_{i\perp}^{*m} (T_{i\perp}^{-m} - T_{i\perp}^{+m}) - v_{i\perp}^{-m} T_{i\perp}^{-m} + v_{i\perp}^{+m} T_{i\perp}^{+m}, \end{aligned} \quad (47)$$

where it has been used that, by definition, $v_{i\perp}^{\pm m}$, $T_{i\perp}^{\pm m}$, $v_{i\perp}^{*m}$, and $T_{i\perp}^{*m}$ are orthogonal to n_i^m . Substituting in the numerical flux expressions (40)–(43) gives

$$\begin{aligned} & (v_i^{-m} - v_i^{+m}) T_i^{*m} + v_i^{*m} (T_i^{-m} - T_i^{+m}) - v_i^{-m} T_i^{-m} + v_i^{+m} T_i^{+m} \\ &= -\alpha k_p^m \left(Z_p^{-m} Z_p^{+m} (v_{\parallel}^{-m} - v_{\parallel}^{+m})^2 + (T_{\parallel}^{-m} - T_{\parallel}^{+m})^2 \right) \\ &- \sum_{i=1}^3 \alpha k_s^m \left(Z_s^{-m} Z_s^{+m} (v_{i\perp}^{-m} - v_{i\perp}^{+m})^2 + (T_{i\perp}^{-m} - T_{i\perp}^{+m})^2 \right). \end{aligned} \quad (48)$$

A similar calculation for the boundary mortar elements, gives that the integrand of (34) is

$$v_i^{-m} T_i^{*m} + v_i^{*m} T_i^{-m} - v_i^{-m} T_i^{-m} = -\alpha \frac{(T_{\parallel}^{-m})^2}{Z_p^{-m}} - \sum_{i=1}^3 \alpha \frac{(T_{i\perp}^{-m})^2}{Z_s^{-m}}. \quad (49)$$

Thus for both (33) and (34) the integrand is non-positive if $\alpha \geq 0$, and the flux yields a stable scheme by Theorem 2.

Corollary 1 *For a variable coefficient, isotropic material the skew-symmetric scheme (26)–(27) using numerical flux (37) with (40)–(43) leads to a semi-discrete scheme that satisfies $\mathcal{E}(t) \leq \mathcal{E}(0)$.*

4.3 Quadrature Integration

We now turn to the case when quadrature is used to evaluate the integrals in the (26)–(27), and show that this has semidiscrete stability even with some variational crimes. In the analysis that follows, we make minimal assumptions about the quadrature rules and interpolation procedures, and the analysis is independent of element shape.

A quadrature based version of (26)–(27) is: For each $e \in \mathbb{E}$, find $\mathbf{v}_j^e \in \hat{V}^e$ and symmetric $\sigma_{ij}^e = \sigma_{ji}^e \in \hat{V}^e$ such that:

$$\mathbf{M}_\rho^e \frac{d\mathbf{v}_i^e}{dt} = - (\mathbf{S}_j^e)^T \sigma_{ij}^e + \sum_{m \in \mathbb{M}^e} (\mathbf{P}^{m,e})^T \mathbf{W}^m \mathbf{T}_i^{*m,e}, \quad (50)$$

$$\mathbf{M}_{S_{ijkl}}^e \frac{d\sigma_{kl}^e}{dt} = \frac{1}{2} (\mathbf{S}_j^e \mathbf{v}_i^e + \mathbf{S}_i^e \mathbf{v}_j^e) + \sum_{m \in \mathbb{M}^e} (\mathbf{P}_{n_j}^{m,e})^T \mathbf{W}^m (\mathbf{v}_i^{*m} - \mathbf{P}^{m,e} \mathbf{v}_i^e). \quad (51)$$

Here, the subscript n_j in $\mathbf{P}_{n_j}^{m,e}$ denotes the fact that this projection operator could be defined such that the unit normal n_j is multiplied before or after the projection, that is $\mathbf{P}_{n_j}^{m,e} \sigma_{ij}^e$ approximates $(n_j \sigma_{ij})^{m,e}$ at the quadrature nodes; see discussion following (26)–(27). The remaining notation in (50)–(51) is discussed in §3.3.

The energy in element $e \in \mathbb{E}$ is defined as

$$\mathcal{E}^e = \frac{1}{2} (\mathbf{v}_i^e)^T \mathbf{M}_\rho^e \mathbf{v}_i^e + \frac{1}{2} (\sigma_{ij}^e)^T \mathbf{M}_{S_{ijkl}}^e \sigma_{kl}^e, \quad (52)$$

with the total energy in the system defined as $\mathcal{E} = \sum_{e \in \mathbb{E}} \mathcal{E}^e$. For this to be a well-defined norm, it is required that \mathbf{M}_ρ^e and \mathbf{M}_S^e , see (21), be symmetric positive definite.

The time derivative of the energy gives

$$\frac{d\mathcal{E}^e}{dt} = \sum_{m \in \mathbb{M}^e} \frac{d\mathcal{E}^{m,e}}{dt}, \quad (53)$$

$$\frac{d\mathcal{E}^{m,e}}{dt} = (\mathbf{v}_i^{m,e})^T \mathbf{W}^m \mathbf{T}_i^{*m,e} + (\mathbf{v}_i^{*m})^T \mathbf{W}^m \mathbf{T}_i^{m,e} - (\mathbf{v}_i^{m,e})^T \mathbf{W}^m \mathbf{T}_i^{m,e}, \quad (54)$$

where $\mathbf{v}_i^{m,e} = \mathbf{P}^{m,e} \mathbf{v}_i^e$ and $\mathbf{T}_i^{m,e} = \mathbf{P}_{n_j}^{m,e} \sigma_{ij}^e$. Considering only a single mortar element $m \in \mathbb{M}$ and summing contributions from all elements that overlap with the mortar gives

$$\frac{d\mathcal{E}^m}{dt} = \sum_{e \in \mathbb{E}^m} \frac{d\mathcal{E}^{m,e}}{dt}, \quad (55)$$

which for an interior mortar element is

$$\begin{aligned} \frac{d\mathcal{E}^m}{dt} &= (\mathbf{v}_i^{-m} - \mathbf{v}_i^{+m})^T \mathbf{W}^m \mathbf{T}_i^{*m} + (\mathbf{v}_i^{*m})^T \mathbf{W}^m (\mathbf{T}_i^{-m} - \mathbf{T}_i^{+m}) \\ &\quad - (\mathbf{v}_i^{-m})^T \mathbf{W}^m \mathbf{T}_i^{-m} + (\mathbf{v}_i^{+m})^T \mathbf{W}^m \mathbf{T}_i^{+m} \end{aligned} \quad (56)$$

and for a boundary mortar element is

$$\frac{d\mathcal{E}^m}{dt} = \left(\mathbf{v}_i^{-m}\right)^T \mathbf{W}^m \mathbf{T}_i^{*m} + \left(\mathbf{v}_i^{*m}\right)^T \mathbf{W}^m \mathbf{T}_i^{-m} - \left(\mathbf{v}_i^{-m}\right)^T \mathbf{W}^m \mathbf{T}_i^{-m}. \quad (57)$$

Here the plus and minus side states on the mortar are defined as

$$\mathbf{v}_i^{\pm m} = \sum_{e \in \mathbb{E}^{\pm m}} \mathbf{v}_i^{m,e}, \quad \mathbf{T}_i^{\pm m} = \mp \sum_{e \in \mathbb{E}^{\pm m}} \mathbf{T}_i^{m,e}. \quad (58)$$

The traction component of the numerical flux is defined as $\mathbf{T}_i^{*m} = \mathbf{T}_i^{*m,e}$ is $e \in \mathbb{E}^{-m}$ and $\mathbf{T}_i^{*m} = -\mathbf{T}_i^{*m,e}$ is $e \in \mathbb{E}^{+m}$.

Theorem 3 *Given a numerical flux such that the integrand of the energy rate (33) and (34) are non-positive, then (56) and (57) are non-positive and quadrature-based discontinuous Galerkin method (50)–(51) satisfies the energy estimate $\mathcal{E}(t) \leq \mathcal{E}(0)$ and is energy stable.*

Proof Recall that \mathbf{W}^m is a diagonal matrix of quadrature weights and surface Jacobians, thus (56) can be written as

$$\frac{d\mathcal{E}^m}{dt} = \sum_{n=1}^{n_q^m} \omega_n \left\{ S_J^m \left(\left(v_i^{-m} - v_i^{+m} \right) T_i^{*m} + v_i^{*m} \left(T_i^{-m} - T_i^{+m} \right) - v_i^{-m} T_i^{-m} + v_i^{+m} T_i^{+m} \right) \right\}_n, \quad (59)$$

and (57) as

$$\frac{d\mathcal{E}^m}{dt} = \sum_{k=1}^{n_q^m} \omega_k \left\{ S_J^m \left(v_i^{-m} T_i^{*m} + v_i^{*m} T_i^{-m} - v_i^{-m} T_i^{-m} \right) \right\}_k, \quad (60)$$

where $\{\cdot\}_k$ denotes that the term inside the brackets is evaluated at mortar quadrature node k . Since the terms inside the brackets are the same as the integrand of (33) and (34), a numerical flux that results in non-positive integrands for (33) and (34) will result in (56) and (57) being non-positive. The remainder of the proof is identical to the proof of Theorem 2. \square

4.4 Comment on the implementation of (51)

Due to the implied summation on the right-hand side (51) the mass matrix to be inverted is not $\mathbf{M}_{S_{ijkl}}^e$ but the combined matrix $\bar{\mathbf{M}}_S^e$ defined in (21). In the results section, we will be using tensor product hexahedral elements with Legendre-Gauss-Lobatto quadrature. With this, mass matrix $\mathbf{M}_{S_{ijkl}}^e = \mathbf{M}^e \mathbf{S}_{ijkl}^e$ is diagonal with \mathbf{M}^e being a diagonal matrix of quadrature weights and Jacobian determinants and \mathbf{S}_{ijkl}^e being a diagonal matrix of the compliance tensor evaluated at the quadrature nodes

(not to be confused with the stiffness matrix \mathbf{S}_i^e). In this case, the combined mass matrix is

$$\bar{\mathbf{M}}_S^e = \bar{\mathbf{S}}^e (\mathbf{I}_{6 \times 6} \otimes \mathbf{M}^e) = (\mathbf{I}_{6 \times 6} \otimes \mathbf{M}^e) \bar{\mathbf{S}}^e, \quad (61)$$

$$\bar{\mathbf{S}}^e = \begin{bmatrix} \mathbf{S}_{1111}^e & \mathbf{S}_{1122}^e & \mathbf{S}_{1133}^e & 2\mathbf{S}_{1123}^e & 2\mathbf{S}_{1113}^e & 2\mathbf{S}_{1112}^e \\ \mathbf{S}_{1122}^e & \mathbf{S}_{2222}^e & \mathbf{S}_{2233}^e & 2\mathbf{S}_{2223}^e & 2\mathbf{S}_{2213}^e & 2\mathbf{S}_{2212}^e \\ \mathbf{S}_{1133}^e & \mathbf{S}_{2233}^e & \mathbf{S}_{3333}^e & 2\mathbf{S}_{3323}^e & 2\mathbf{S}_{3313}^e & 2\mathbf{S}_{3312}^e \\ 2\mathbf{S}_{1123}^e & 2\mathbf{S}_{2223}^e & 2\mathbf{S}_{3323}^e & 4\mathbf{S}_{2323}^e & 4\mathbf{S}_{2313}^e & 4\mathbf{S}_{2312}^e \\ 2\mathbf{S}_{1113}^e & 2\mathbf{S}_{2213}^e & 2\mathbf{S}_{3313}^e & 4\mathbf{S}_{2313}^e & 4\mathbf{S}_{1313}^e & 4\mathbf{S}_{1312}^e \\ 2\mathbf{S}_{1112}^e & 2\mathbf{S}_{2212}^e & 2\mathbf{S}_{3312}^e & 4\mathbf{S}_{2312}^e & 4\mathbf{S}_{1312}^e & 4\mathbf{S}_{1212}^e \end{bmatrix}, \quad (62)$$

Additionally, the inverse of the combined mass matrix is

$$(\bar{\mathbf{M}}_S^e)^{-1} = \bar{\mathbf{M}}_C^e = \bar{\mathbf{C}}^e (\mathbf{I}_{6 \times 6} \otimes (\mathbf{M}^e)^{-1}) = (\mathbf{I}_{6 \times 6} \otimes (\mathbf{M}^e)^{-1}) \bar{\mathbf{C}}^e, \quad (63)$$

$$\bar{\mathbf{C}}^e = \begin{bmatrix} \mathbf{C}_{1111}^e & \mathbf{C}_{1122}^e & \mathbf{C}_{1133}^e & \mathbf{C}_{1123}^e & \mathbf{C}_{1113}^e & \mathbf{C}_{1112}^e \\ \mathbf{C}_{1122}^e & \mathbf{C}_{2222}^e & \mathbf{C}_{2233}^e & \mathbf{C}_{2223}^e & \mathbf{C}_{2213}^e & \mathbf{C}_{2212}^e \\ \mathbf{C}_{1133}^e & \mathbf{C}_{2233}^e & \mathbf{C}_{3333}^e & \mathbf{C}_{3323}^e & \mathbf{C}_{3313}^e & \mathbf{C}_{3312}^e \\ \mathbf{C}_{1123}^e & \mathbf{C}_{2223}^e & \mathbf{C}_{3323}^e & \mathbf{C}_{2323}^e & \mathbf{C}_{2313}^e & \mathbf{C}_{2312}^e \\ \mathbf{C}_{1113}^e & \mathbf{C}_{2213}^e & \mathbf{C}_{3313}^e & \mathbf{C}_{2313}^e & \mathbf{C}_{1313}^e & \mathbf{C}_{1312}^e \\ \mathbf{C}_{1112}^e & \mathbf{C}_{2212}^e & \mathbf{C}_{3312}^e & \mathbf{C}_{2312}^e & \mathbf{C}_{1312}^e & \mathbf{C}_{1212}^e \end{bmatrix}, \quad (64)$$

where \mathbf{C}_{ijkl}^e is the diagonal matrix of stiffness tensor elements C_{ijkl} evaluated at the quadrature nodes. With this, for tensor product elements, (51) is equivalently written as

$$\begin{aligned} \mathbf{M}^e \frac{d\boldsymbol{\sigma}_{kl}^e}{dt} &= \frac{1}{2} \mathbf{C}_{ijkl}^e (\mathbf{S}_k^e \mathbf{v}_l^e + \mathbf{S}_l^e \mathbf{v}_k^e) \\ &+ \sum_{m \in \mathbb{M}^e} \mathbf{C}_{ijkl}^e (\mathbf{P}_{n_k}^{m,e})^T \mathbf{W}^m (\mathbf{v}_l^{*m} - \mathbf{P}^{m,e} \mathbf{v}_l^e), \end{aligned} \quad (65)$$

where we highlight that \mathbf{C}_{ijkl}^e is defined on the volume element and not the mortar.

For many element types such a decomposition is not possible because the interpolation and quadrature points are different. One option in this case is to invert $\bar{\mathbf{M}}_S^e$ on each element. Alternatively, one could use the weight-adjusted approach of Chan [6] and let

$$\bar{\mathbf{M}}_S^e = (\mathbf{I}_{6 \times 6} \otimes \mathbf{M}^e) (\bar{\mathbf{M}}_C^e)^{-1} (\mathbf{I}_{6 \times 6} \otimes \mathbf{M}^e), \quad (66)$$

which then allows (51) to be written as

$$\begin{aligned} \mathbf{M}^e \frac{d\boldsymbol{\sigma}_{kl}^e}{dt} &= \frac{1}{2} \mathbf{M}_{C_{ijkl}}^e (\mathbf{M}^e)^{-1} (\mathbf{S}_k^e \mathbf{v}_l^e + \mathbf{S}_l^e \mathbf{v}_k^e) \\ &+ \sum_{m \in \mathbb{M}^e} \mathbf{M}_{C_{ijkl}}^e (\mathbf{M}^e)^{-1} (\mathbf{P}_{n_k}^{m,e})^T \mathbf{W}^m (\mathbf{v}_l^{*m} - \mathbf{P}^{m,e} \mathbf{v}_l^e); \end{aligned} \quad (67)$$

the weight adjusted approach can also be used for the case of non-constant Jacobians when the mass matrix \mathbf{M}^e is not diagonal [7].

4.5 Comparison with a Previous DG Mortar Method

Here we compare the proposed method with the approach outlined by Kopriva [14] and Kopriva, Woodruff, and Hussaini [17], which was analyzed by Bui-Thanh and Ghattas [3]. In this previous approach, the fluxes are computed on the mortar, but they are projected back to the local element space for integration. This is as opposed to our approach where we project the test and trial functions to the mortar space, and all surface integrals are computed on the mortar.

In this earlier approach, method (26)–(27) would be

$$\int_{\hat{e}} J^e \rho \phi_i \frac{\partial v_i^e}{\partial t} = - \int_{\hat{e}} J^e \frac{\partial \phi_i}{\partial x_j} \sigma_{ij}^e + \int_{\partial \hat{e}} S_J \phi_i^e T_i^{*e}, \quad (68)$$

$$\begin{aligned} \int_{\hat{e}} J^e \psi_{ij} S_{ijkl} \frac{\partial \sigma_{kl}^e}{\partial t} &= \int_{\hat{e}} \frac{J^e}{2} \psi_{ij} \left(\frac{\partial v_i^e}{\partial x_j} + \frac{\partial v_j^e}{\partial x_i} \right) \\ &\quad + \int_{\partial \hat{e}} S_J n_j^e \psi_{ij}^e (v_i^{*e} - v_i^e). \end{aligned} \quad (69)$$

The numerical flux terms T_i^{*e} and v_i^{*e} are the L^2 -projected fluxes from the mortar onto the surface of the volume element, e.g., L^2 -projection from the set of mortar elements \mathbb{M}^e .

With exact integration and L^2 -projection, this scheme has the same stability properties as (26)–(27), but when inexact quadrature is used this scheme may admit energy growth (even on affine elements). In the case of affine meshes with constant coefficients, Bui-Thanh and Ghattas [3] showed that Legendre-Gauss-Lobatto (LGL) integration leads to an energy estimate of the form $\mathcal{E}(t) \leq e^{ct} \mathcal{E}(0)$ where $c > 0$ is a small but positive constant that converges to zero under mesh refinement. Thus, even though stable the scheme admits exponential energy growth.

The main difficulty in achieving a strictly non-increasing energy estimate for this scheme is that when quadrature is used, the inexact face mass matrix and L^2 -projection operator are no longer consistent. This means that integrals over the element face space and the mortar space are not equivalent. One approach to overcoming these difficulties would be to use an inexact L^2 -projections defined such that the quadrature version of (68)–(69) is purely dissipative. With some reformation, the proposed scheme (50)–(51) could be interpreted as giving a consistent approach for defining these inexact L^2 -projections.

5 Computational Results

In this section, the energy stability of the proposed mortar method is verified for $d = 3$ for isotropic elasticity and the accuracy of the scheme is investigated. The adapted meshes in the examples are generated with `p4est` [4] using its topology iterator [12]. Hexahedral elements with tensor product Legendre-Gauss-Lobatto (LGL) nodes are used for interpolation and integration (e.g., the so-called discontinuous Galerkin spectral element method [2, 15]); LGL quadrature is also used on the mortar elements. A computational advantage of LGL quadrature is that some of the degrees of freedom exist on the element faces which means that for conforming faces,

no interpolation operation is required to compute the flux (obviously interpolation is required for non-conforming faces). That said, an LGL quadrature rule with $N + 1$ points can only integrate polynomials of degree $2N - 1$ exactly, and thus the diagonal mass matrix defined using LGL quadrature is inexact for two polynomials of degree N . When curved elements and variable coefficients are used, the metric terms and material properties are multiplied with the quadrature weights, thus maintaining the diagonal structure of the mass matrix (leading to further under-integration). Despite this, as shown above, the newly proposed method does not require exact integration as stability is achieved through the use of skew-symmetry. The geometry terms are approximated in an isoparametric fashion (i.e., the coordinate mapping is evaluated at the interpolation nodes of the reference element) with the metric terms evaluated using the curl invariant form of Kopriva [13].

All of the schemes introduced above are in semi-discrete form with time left continuous, and the scheme can be written as a linear ordinary differential equations:

$$\frac{d\mathbf{q}}{dt} = \mathbf{A}\mathbf{q}, \quad (70)$$

where \mathbf{q} is the vector of stresses and particle velocities at all the degrees of freedom; as is standard for hyperbolic equation, in our implementation \mathbf{A} is not explicitly formed only its action on \mathbf{q} is computed. We integrate (70) in time using the fourth order, low-storage, Runge-Kutta scheme of Carpenter Kennedy [5] (scheme 5[4], solution 3). In order to compute the time step for the Runge-Kutta method, at every node of the mesh we compute

$$\beta = \min(\beta_1, \beta_2, \beta_3), \quad (71)$$

$$\beta_k = \left(N \sqrt{C_p \frac{\partial r_k}{\partial x_i} \frac{\partial r_k}{\partial x_i}} \right)^{-1} \quad (\text{no summation over } k), \quad (72)$$

where N is the polynomial order and $C_p = \sqrt{(\lambda + 2\mu)/\rho}$ is the p-wave speed of the material at the node. The maximum time step is then chosen to be the minimum β over the whole mesh.

5.1 Planewave Solution in Periodic Box

In this test, the newly proposed skew-symmetric formulation is compared with the previously proposed approach of Kopriva. To do this, an affine mesh with constant material properties is considered. Subsequent tests of the newly proposed approach will involved variable material properties and non-affine meshes.

The domain is taken to be the unit cube: $\Omega = [0, 1]^3$. The domain is initially partitioned into a $2 \times 2 \times 2$ mesh of hexahedral elements, and then four elements are further subdivided into 8 elements; see Fig. 2. This base mesh has $E = 36$ elements, and in the base mesh only faces internal to the refined blocks are conforming.

The material is taken to be homogeneous, isotropic with $\rho = 2$, $\mu = 3$, and $\lambda = 4$. The solution is a planewave propagating in the x_1 -direction:

$$u_1 = \cos(2\pi(c_p t + x_1)), \quad u_2 = \cos(2\pi(c_s t + x_1)), \quad u_3 = \cos(2\pi(c_s t + x_1)), \quad (73)$$

E	Projection error (rate)	Interpolation error (rate)	Kopriva Projection error (rate)	Kopriva Interpolation error (rate)
Polynomial order $N = 3$				
36	1.9×10^0	1.8×10^0	1.7×10^0	1.7×10^0
288	5.6×10^{-2} (5.1)	5.5×10^{-2} (5.0)	4.9×10^{-2} (5.1)	4.9×10^{-2} (5.1)
2304	1.4×10^{-3} (5.3)	1.4×10^{-3} (5.3)	1.2×10^{-3} (5.3)	1.2×10^{-3} (5.3)
18432	8.8×10^{-5} (4.0)	8.9×10^{-5} (4.0)	6.6×10^{-5} (4.2)	6.6×10^{-5} (4.2)
147456	7.5×10^{-6} (3.5)	8.6×10^{-6} (3.4)	4.7×10^{-6} (3.8)	4.7×10^{-6} (3.8)
1179648	6.9×10^{-7} (3.4)	9.6×10^{-7} (3.2)	3.6×10^{-7} (3.7)	3.6×10^{-7} (3.7)
Polynomial order $N = 4$				
36	1.1×10^{-1}	1.1×10^{-1}	9.5×10^{-2}	9.6×10^{-2}
288	1.3×10^{-3} (6.5)	1.2×10^{-3} (6.5)	1.1×10^{-3} (6.5)	1.1×10^{-3} (6.5)
2304	4.3×10^{-5} (4.9)	4.3×10^{-5} (4.8)	3.5×10^{-5} (5.0)	3.4×10^{-5} (5.0)
18432	1.8×10^{-6} (4.6)	1.9×10^{-6} (4.5)	1.2×10^{-6} (4.9)	1.2×10^{-6} (4.8)
147456	7.7×10^{-8} (4.5)	9.8×10^{-8} (4.3)	4.3×10^{-8} (4.8)	4.3×10^{-8} (4.8)
Polynomial order $N = 5$				
36	4.2×10^{-3}	4.0×10^{-3}	3.5×10^{-3}	3.4×10^{-3}
288	7.6×10^{-5} (5.8)	7.4×10^{-5} (5.8)	6.5×10^{-5} (5.8)	6.4×10^{-5} (5.7)
2304	1.5×10^{-6} (5.7)	1.5×10^{-6} (5.6)	1.2×10^{-6} (5.8)	1.2×10^{-6} (5.8)
18432	3.1×10^{-8} (5.6)	3.5×10^{-8} (5.4)	2.2×10^{-8} (5.8)	2.1×10^{-8} (5.8)
147456	6.8×10^{-10} (5.5)	9.3×10^{-10} (5.2)	4.1×10^{-10} (5.7)	4.1×10^{-10} (5.7)
Polynomial order $N = 6$				
36	5.2×10^{-4}	5.2×10^{-4}	4.7×10^{-4}	4.7×10^{-4}
288	4.4×10^{-6} (6.9)	4.3×10^{-6} (6.9)	3.7×10^{-6} (7.0)	3.6×10^{-6} (7.0)
2304	4.3×10^{-8} (6.7)	4.5×10^{-8} (6.6)	3.2×10^{-8} (6.8)	3.2×10^{-8} (6.8)
18432	4.6×10^{-10} (6.5)	5.4×10^{-10} (6.4)	3.0×10^{-10} (6.7)	3.0×10^{-10} (6.7)
Polynomial order $N = 7$				
36	3.9×10^{-5}	3.7×10^{-5}	3.1×10^{-5}	3.0×10^{-5}
288	2.2×10^{-7} (7.5)	2.2×10^{-7} (7.4)	1.8×10^{-7} (7.4)	1.8×10^{-7} (7.4)
2304	1.2×10^{-9} (7.5)	1.2×10^{-9} (7.5)	9.4×10^{-10} (7.6)	9.4×10^{-10} (7.6)

Table 1 Error and estimated convergence rates for a planewave propagating through an adapted, affine mesh.

with $c_p = \sqrt{(\lambda + 2\mu)/\rho}$ and $c_s = \sqrt{\mu/\rho}$ being the P- and S-wave speeds of the material. Here the solution is written in terms of the displacements, and the velocity and stresses are

$$v_i = \frac{\partial u_i}{\partial t}, \quad \sigma_{ij} = \lambda \delta_{ij} \frac{\partial u_k}{\partial x_k} + \mu \left(\frac{\partial u_i}{\partial x_j} + \frac{\partial u_j}{\partial x_i} \right). \quad (74)$$

Table 1 and Fig. 2 show convergence results for this planewave test for varying polynomial order N ; refinement of the mesh is done with bisection so that each hexahedral element is subdivided into 8 affine elements of equal size. The final time of the simulation is $t = 20/c_s$, e.g., the planewave propagates around the unit cube 20 times. As Table 1 shows, four methods are considered for each N . For the columns labeled *Projection* and *Kopriva Projection* the mortar conforms to the larger element (as in the center panel of Fig. 1), because the solution from the smaller elements has to be projected to the mortar. For the columns labeled *Interpolation* and *Kopriva Interpolation* the mortar conforms to the smaller elements (as in the

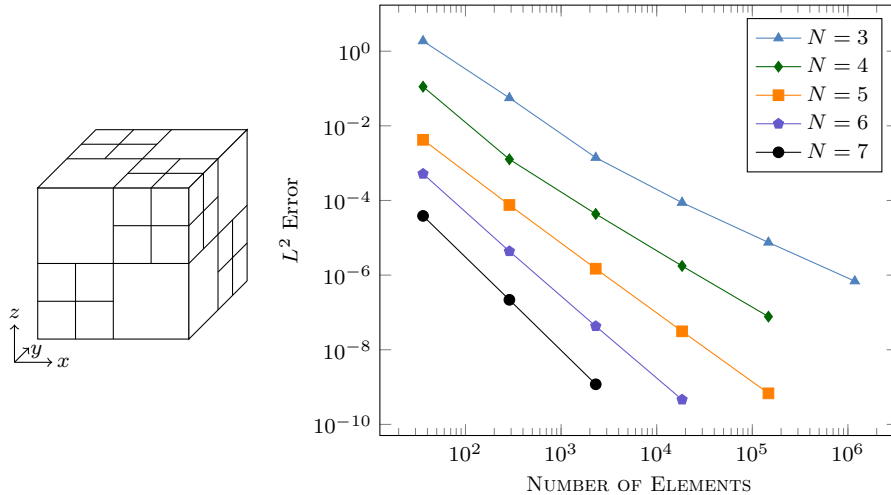


Fig. 2 (left) Base mesh for planewave test. (right) Log-log plot of E (number of elements) versus the L^2 error (measured with the energy norm) for a mesh of affine (square) elements. Only the error for the projection mortar is shown as the other three cases look similar.

right panel of Fig. 1), and the solution from the large element is interpolated to the mortar. The columns *Projection* and *Interpolation* refer to the method (50)–(51), whereas the columns *Kopriva Projection* and *Kopriva Interpolation* refer to the method described in §4.5. In all cases, the error in the solution is measured using the quadrature based energy norm (52). The numerical flux used for this tests is the upwind flux described by (37)–(44) with $\alpha = 1$.

As can be seen Table 1, all four methods converge at high-rates. That said, the two Kopriva methods do have lower errors and improved rates for the considered problem. The two newly proposed methods seem to be tending towards convergence rates at order N (as opposed to $N + 1/2$), suggesting that some accuracy is lost with the improved stability properties.

5.2 Eigenvalue Spectrum and Long-Time Energy Stability

To highlight the stability properties of the methods, we now consider the eigenvalue spectrum of each of the methods using the mesh and material properties of the previous periodic box test problem. Fig. 3 shows the eigenvalue spectrum for all the methods with an upwind flux on the base mesh ($E = 36$) with polynomial; the spectrum is computed by forming the matrix \mathbf{A} and then finding the eigenvalues with the MATLAB [1] `eig` command. Table 2 gives the maximum and minimum real part of the eigenvalue spectrum for all four methods with both the upwind ($\alpha = 1$) and central ($\alpha = 0$) flux. As can be seen, the Projection and Interpolation methods are stable (in the sense that the maximum, real part of the eigenvalue spectrum is close to zero) consistent with the energy analysis earlier in the paper. The two Kopriva methods have positive real parts, even with the upwind flux, consistent

	$\max_k \Re(\lambda_k)$	$\min_k \Re(\lambda_k)$	$\max_k \Im(\lambda_k) $
		Upwind Flux	
Projection	6.91×10^{-13}	-5.66×10^2	4.25×10^2
Interpolation	4.81×10^{-13}	-3.07×10^2	1.47×10^2
Kopriva Projection	7.19×10^{-05}	-3.06×10^2	1.73×10^2
Kopriva Interpolation	6.40×10^{-04}	-3.07×10^2	1.47×10^2
		Central Flux	
Projection	1.58×10^{-12}	-9.32×10^{-13}	4.89×10^2
Interpolation	1.10×10^{-12}	-8.08×10^{-13}	2.07×10^2
Kopriva Projection	8.57×10^{-1}	-8.57×10^{-1}	2.08×10^2
Kopriva Interpolation	1.15×10	-1.15×10	2.07×10^2

Table 2 Table comparing the extrema of the real and imaginary parts of the eigenvalue spectrum for all four methods with both an upwind and central flux with $N = 4$ on the base mesh ($E = 36$). Eigenvalues are computed by forming the matrix and using the MATLAB [1] `eig` command.

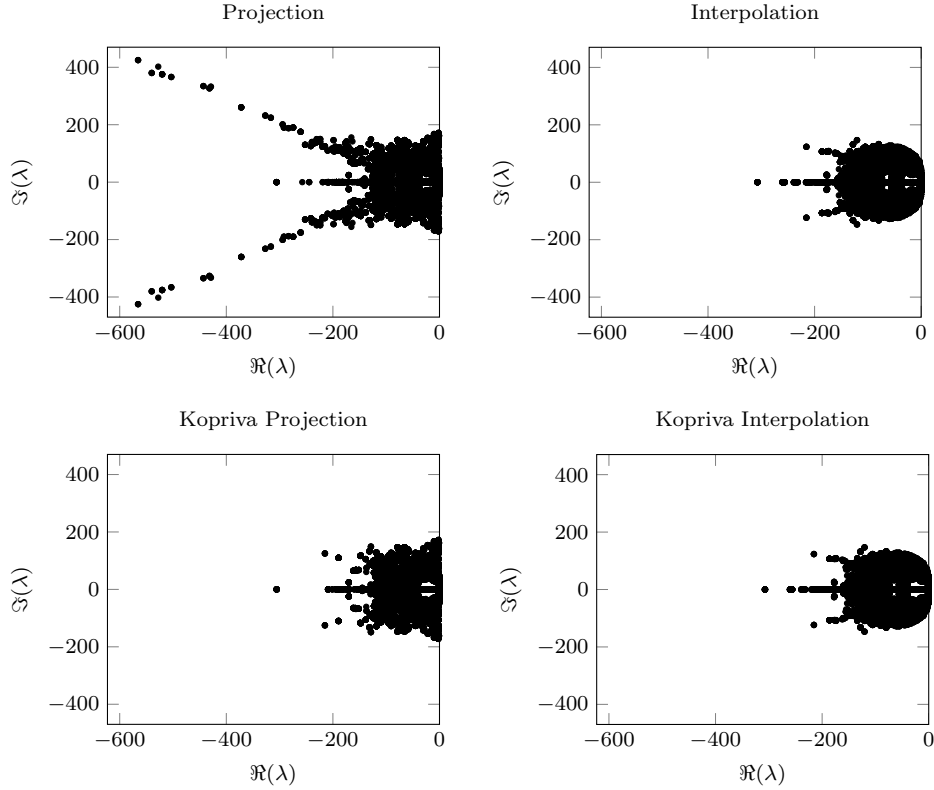


Fig. 3 Eigenvalue spectrum for the $E = 36$ mesh with polynomial order $N = 4$ upwind flux.

with the energy analysis of Bui-Thanh and Ghattas which allows for energy growth (e.g., a positive, real part of the spectrum). For this mesh, which has a total of 40500 degrees of freedom, the Kopriva projection and interpolation methods with the upwind flux have, respectively, 18 and 12 computed eigenvalues that have a real part larger than 10^{-12} .

As can be seen from both the figure and table, the spectral radius of the projection method is larger than the Interpolation method (2.3 times larger with the upwind flux and 2.4 times larger with the central flux). The implication of this is that the largest time step that can be used for the Projection method (on this mesh) is almost half the size of that of the Interpolation method. Given that this particular mesh has a very high non-conforming to conforming ratio, 2/3 of the mortar is non-conforming, it is unclear whether this stiffness would be seen in practical simulations. For the upwind flux, both the Projection and Kopriva Projection methods have twice as many eigenvalues with approximately zero real part as compared with the Interpolation and Kopriva Interpolation methods (~ 8300 versus ~ 4200 eigenvalues with real component less than 10^{-12} in magnitude). This suggests that the Projection and Kopriva Projection methods are slightly less dissipative across the non-conforming interfaces.

To further explore the energy stability of the newly proposed methods, an adapted spherical shell is considered. The spherical shell is initially meshed using 6 hexahedral elements, and these elements are then randomly refined to produce a non-conforming base mesh with $E = 745$ elements. Since the the common (hexahedral) decomposition of a spherical shell would result in one of the grid lines being aligned with the radial direction, the complexity of the problem is increased by rotating the outside of the shell by 1 radian with respect to the inside of the shell (along the polar angle). A cross-section through the center of the sphere of the resulting adapted mesh is shown in Fig. 5. Though the domain is conforming at the continuous level, the mesh will be discretely discontinuous across non-conforming faces as each element samples the non-polynomial geometry transformation differently.

At every degree of freedom of the mesh the material properties are randomly assigned which results in a discontinuous, non-smooth description; the S-wave and P-wave speeds vary from 4.4 to 6.4 and 7.2 to 10.6, respectively. Similarly, the initial condition is randomly generated. This is done to widely distribute the energy in the solution across various eigenmodes of the operator. The simulation is then run to time $t = 1000$, which since the inner and outer radii of the shell are 7.9 and 14.5, this allows waves propagate around the shell hundreds of times; these inner and outer radii are chosen to be the same as the next test problem.

Fig. 4 shows the energy in the solution versus time for both the Projection and Interpolation methods with the upwind and central fluxes. As can be seen, the upwind schemes quickly dissipated energy in the unresolved modes in the solution and then remain stable. The central method preserves the initial energy; there is an $\sim 0.1\%$ energy lose for both central schemes but this is likely from dissipation from the Runge-Kutta scheme.

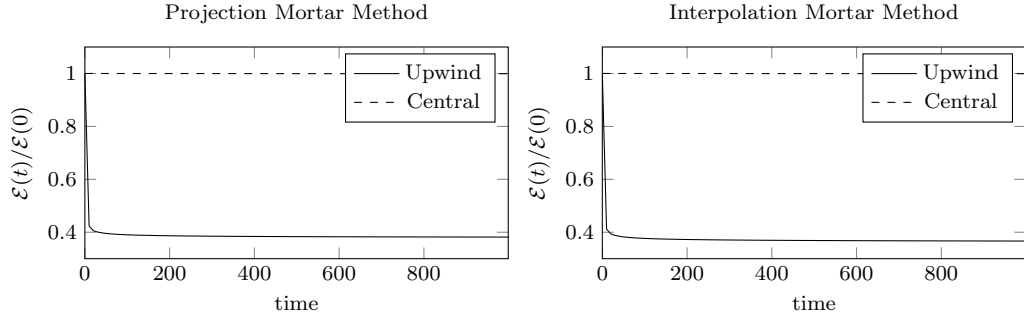


Fig. 4 Energy dissipation in a randomly, heterogeneous spherical shell comparing. Shown are both the Projection and Interpolation methods with the upwind ($\alpha = 1$) and central ($\alpha = 0$) flux.

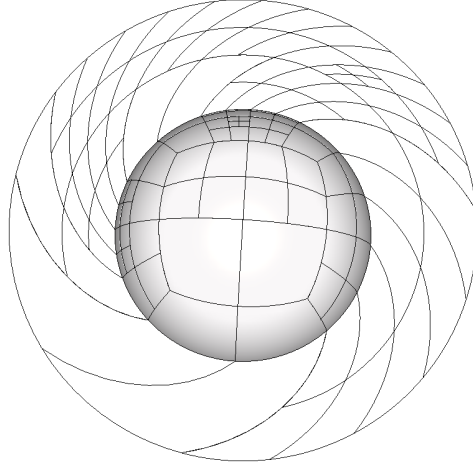


Fig. 5 Cross-section of the base mesh for the spherical shell test problem showing both the random refinement and the rotation of outside of the shell with respect to the inside. Total number of elements in the base mesh is $E = 745$.

5.3 Mode of a Heterogeneous Spherical Shell

In this test the previously described spherical shell (with random refinement) is considered, but now the material properties are taken to be

$$\rho = 2 + \cos\left(\frac{2\pi r}{10}\right), \quad \mu = \frac{50}{10+r}, \quad \lambda = 10 \exp\left(\frac{-r}{10}\right); \quad (75)$$

see also the left panel of Fig. 6. To derive a modal solution with these material parameters, it is assumed the when written in spherical coordinates, only the radial displacement is non-zero. The radial displacement is taken to be of the form

$$u_r = \cos(t)\phi(r), \quad (76)$$

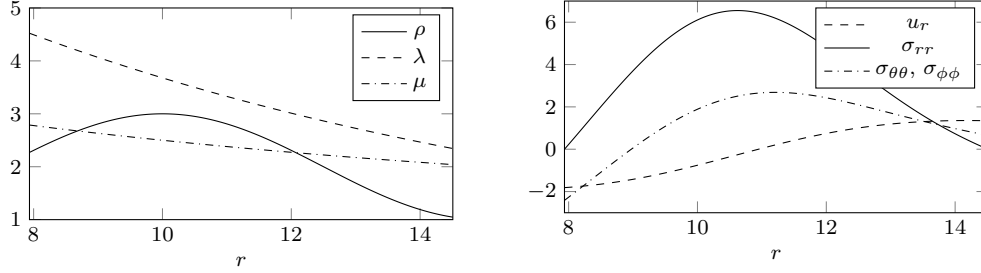


Fig. 6 (left) Material properties as a function of r for the spherical shell test problem. (right) Non-zero, modal solution fields (in spherical coordinates) at time $t = 0$ for the spherical shell test problem.

E	$N = 4$ error (rate)	$N = 5$ error (rate)	$N = 6$ error (rate)	$N = 7$ error (rate)
Projection Method				
745	8.3×10^{-0}	3.2×10^{-0}	8.7×10^{-1}	2.3×10^{-1}
5960	3.2×10^{-1} (4.7)	4.9×10^{-2} (6.0)	7.6×10^{-3} (6.8)	1.1×10^{-3} (7.6)
47680	1.1×10^{-2} (4.9)	9.1×10^{-4} (5.7)	7.5×10^{-5} (6.7)	5.5×10^{-6} (7.7)
381440	4.1×10^{-4} (4.7)	1.8×10^{-5} (5.7)	7.5×10^{-7} (6.6)	2.8×10^{-8} (7.6)
Interpolation Method				
745	9.1×10^{-0}	3.5×10^{-0}	8.5×10^{-1}	2.2×10^{-1}
5960	3.4×10^{-1} (4.7)	4.7×10^{-2} (6.2)	7.8×10^{-3} (6.8)	1.4×10^{-3} (7.3)
47680	9.7×10^{-3} (5.1)	9.4×10^{-4} (5.6)	8.3×10^{-5} (6.6)	8.1×10^{-6} (7.5)
381440	3.4×10^{-4} (4.8)	1.7×10^{-5} (5.8)	8.9×10^{-7} (6.6)	1.0×10^{-7} (6.3)

Table 3 Error and estimated convergence rates for the spherical shell using the Projection method with an upwind flux.

e.g., the temporal and spatial dependence are separable. With this, in spherical coordinates the components of the stress tensor are

$$\sigma_{rr} = (\lambda + 2\mu) \frac{\partial u_r}{\partial r} + 2\mu \frac{u_r}{r}, \quad \sigma_{\theta\theta} = \sigma_{\phi\phi} = 2(\lambda + \mu) \frac{u_r}{r} + \lambda \frac{\partial u_r}{\partial r}, \quad (77)$$

with $\sigma_{r\theta} = \sigma_{r\phi} = \sigma_{\theta\phi} = 0$. To solve this the MATLAB package Chebfun [9] is used, and R_1 and R_2 are chosen so that $\sigma_{rr} = 0$ is zero at the inner and outer radii of the shell; see Appendix B for details. The right panel Fig. 6 shows u_r , σ_{rr} , $\sigma_{\theta\theta}$, and $\sigma_{\phi\phi}$ as functions of r at time $t = 0$. To implement the solution, the displacements are first converted to Cartesian coordinates,

$$u_i = \frac{x_i}{r} u_r, \quad (78)$$

where $r = \sqrt{x_i x_i}$ is the radial distance, and then the velocities and stresses are computed using (74).

In Table 3 and Fig. 7 error and convergence results are given for this problem for varying polynomial orders with the Projection mortar method with the upwind flux. The final time for the simulation is $t = 6\pi$, and thus three oscillations of the solution

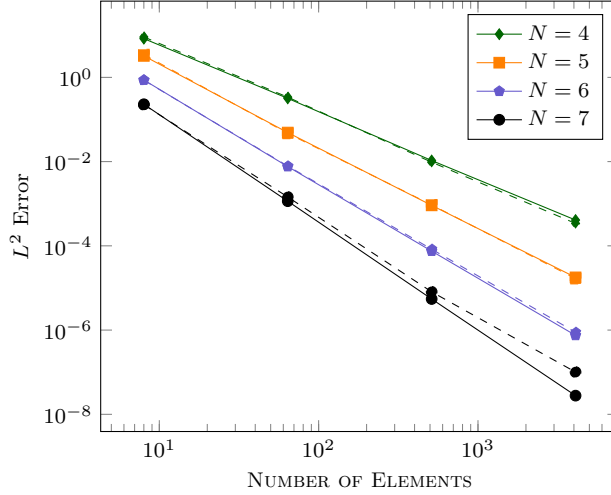


Fig. 7 Log-log plot of E (number of elements) versus the L^2 error (measured with the energy norm) for a mesh the spherical shell test problem for the Projection method (solid lines) and the Interpolation method (dashed lines) with the upwind flux.

have been considered. We also highlight again, that since the geometry transform is non-polynomial across non-conforming interfaces the geometry is discontinuous meaning at the discrete level there are gaps in the mesh.

A Construction of L^2 -projection operators

Here the construction of the mortar projection operators is discussed, namely the construction of $\mathcal{P}^{m,e}$ for some $m \in \mathbb{M}$ and $e \in \mathbb{E}^m$. Of particular interest is when the mortar space does not support all the functions that the connected element faces support. For example, in the center panel of Fig. 1 if mortar m^2 supports polynomials of degree N then it cannot support the discontinuous polynomial which is defined by functions on the connected faces of e^3 and e^4 .

For an $m \in \mathbb{M}$ and $e \in \mathbb{E}^m$, let \hat{m}^e be the portion of the reference mortar element \hat{m} that corresponds to the intersection in physical space of m and ∂e , that is $\hat{m}^e = \mathbf{r}^m(m \cap \partial e)$. The projection operator in $\mathcal{P}^{m,e}$ is then defined so that for a given $q^e \in \hat{V}^e$ the following holds for all $\phi^m \in \hat{U}^m$:

$$\int_{\hat{m}} \phi^m q^{m,e} = \int_{\hat{m}^e} \phi^m q^e, \quad (79)$$

where $q^{m,e} = \mathcal{P}^{m,e} q^e$. In the right-hand side integrand q^e is evaluated on the reference mortar, not the element boundary, and thus $q^e = q^e(\mathbf{x}^e(\mathbf{r}^e(\mathbf{x}^m(\mathbf{r}))))$ with \mathbf{r} being the integration variable. Note the surface Jacobian is not included in the definition of the projection operator given here, and thus the projection operator is defined on the straight-sided reference element.

In the results, exact integration is used to construct $\mathbf{P}^{m,e}$, that is there are no variational crimes in the discrete representation of $\mathcal{P}^{m,e}$ defined from (79) since Legendre-Gauss-Lobatto (LGL) quadrature is not used. Moreover, since the basis functions are tensor product, the L^2 -projection operators can also be constructed as tensor product operators, and only one-dimensional projection operators are needed. Thus, since the non-conforming interfaces in the

results are two-to-one, only projection operators from the bottom, \mathcal{P}_b , and top, \mathcal{P}_t , halves of a 1-D element are required. The bottom and top projection operators then satisfy

$$\int_{-1}^1 \phi \mathcal{P}_b q = \int_{-1}^0 \phi q, \quad \int_{-1}^1 \phi \mathcal{P}_t q = \int_0^1 \phi q, \quad (80)$$

for all polynomials q and ϕ of degree N .

To define the discrete operators \mathbf{P}_b and \mathbf{P}_t , let ϕ be the evaluation of ϕ at the LGL quadrature nodes on the interval $[-1, 1]$. Similarly, let \mathbf{q}_b be the evaluation of q at LGL quadrature nodes once they have been scaled to be between $[-1, 0]$ and \mathbf{I}_b interpolate the ϕ to these same nodes; similar definitions are used for \mathbf{q}_t and \mathbf{I}_t except on the interval $[0, 1]$. Then if \mathbf{M} is the exact mass matrix for integrating two polynomial of degree N evaluated at the LGL quadrature nodes in $[-1, 1]$, then (80) is discretely

$$\phi^T \mathbf{M} \mathbf{P}_b \mathbf{q}_b = \frac{1}{2} \phi^T \mathbf{I}_b^T \mathbf{M} \mathbf{q}_b, \quad \phi^T \mathbf{M} \mathbf{P}_t \mathbf{q}_t = \frac{1}{2} \phi^T \mathbf{I}_t^T \mathbf{M} \mathbf{q}_t, \quad (81)$$

which holds for all ϕ , \mathbf{q}_t , and \mathbf{q}_b and thus

$$\mathbf{P}_b = \frac{1}{2} \mathbf{M}^{-1} \mathbf{I}_b^T \mathbf{M}, \quad \mathbf{P}_t = \frac{1}{2} \mathbf{M}^{-1} \mathbf{I}_t^T \mathbf{M}. \quad (82)$$

B Construction of Modal Solution on the Heterogeneous Spherical Shell

In order to construct a modal solution in the radial heterogeneous spherical shell, the equations of isotropic, elasticity are considered in spherical coordinates. Since only the radial displacement is non-zero, and the displacement is of the form $u_r = \cos(t) \phi(r)$, these reduce to solving the following boundary value problem:

$$0 = \rho \phi + \frac{d\sigma_{rr}}{dr} + \frac{2}{r} \sigma_{rr}, \quad \sigma_{rr} = (\lambda + 2\mu) \frac{d\phi}{dr} + \frac{2}{r} \lambda \phi, \quad (83)$$

with $\sigma_{rr} = 0$ at $r = R_1$ and $r = R_2$. We note that the solution to this problem is not unique and for the test problem we just need to find a particular solution to the equation.

To solve (83) the MATLAB Chebfun package [9] was used. In order to avoid the trivial solution $\phi = 0$ which would satisfy $\sigma_{rr} = 0$ for all r , so instead the initial value problem with values for $\phi(0) = 0$ and $\frac{d\phi}{dr}(0) = -\frac{1}{3}$ and then choose R_1 and R_2 to be the first two roots of the resulting σ_{rr} field. The Chebfun script along with the data necessary for constructing the high-order polynomial interpolant are available at the GitHub repository https://github.com/bfam/spherical_shell.

References

1. MATLAB version 8.6.0.267246 (R2015b). Natick, Massachusetts.
2. K. Black. A conservative spectral element method for the approximation of compressible fluid flow. *Kybernetika*, 35(1):133–146, 1999.
3. T. Bui-Thanh and O. Ghattas. Analysis of an *hp*-nonconforming discontinuous galerkin spectral element method for wave propagation. *SIAM Journal on Numerical Analysis*, 50(3):1801–1826, 2012.
4. Carsten Burstedde, Lucas C. Wilcox, and Omar Ghattas. p4est: Scalable algorithms for parallel adaptive mesh refinement on forests of octrees. *SIAM Journal on Scientific Computing*, 33(3):1103–1133, 2011.
5. M.H. Carpenter and C.A. Kennedy. Fourth-order 2N-storage Runge-Kutta schemes. Technical Report NASA TM-109112, National Aeronautics and Space Administration, Langley Research Center, Hampton, VA, 1994.

6. J. Chan. Weight-adjusted discontinuous Galerkin methods: matrix-valued weights and elastic wave propagation in heterogeneous media. *ArXiv e-prints*, Jan 2017. arXiv1701.00215.
7. J. Chan, R. J. Hewett, and T. Warburton. Weight-adjusted discontinuous Galerkin methods: curvilinear meshes. *ArXiv e-prints*, Aug 2016. arXiv1608.03836.
8. J. Chan, Z. Wang, A. Modave, J.-F. Remacle, and T. Warburton. GPU-accelerated discontinuous Galerkin methods on hybrid meshes. *Journal of Computational Physics*, 318:142–168, 2016.
9. T. A. Driscoll, N. Hale, and L. N. Trefethen, editors. *Chebfun Guide*. Pafnuty Publications, Oxford, 2014.
10. T.C. Fisher, M.H. Carpenter, J. Nordström, N.K. Yamaleev, and C. Swanson. Discretely conservative finite-difference formulations for nonlinear conservation laws in split form: Theory and boundary conditions. *Journal of Computational Physics*, 234:353375, 2013.
11. G. Gassner. A skew-symmetric discontinuous galerkin spectral element discretization and its relation to sbp-sat finite difference methods. *SIAM Journal on Scientific Computing*, 35(3):A1233–A1253, 2013.
12. Tobin Isaac, Carsten Burstedde, Lucas C. Wilcox, and Omar Ghattas. Recursive algorithms for distributed forests of octrees. *SIAM Journal on Scientific Computing*, 37(5):C497–C531, 2015.
13. D. Kopriva. Metric identities and the discontinuous spectral element method on curvilinear meshes. *Journal of Scientific Computing*, 26(3):301–327, 2006.
14. D. A. Kopriva. A conservative staggered-grid Chebyshev multidomain method for compressible flows. II. A semi-structured method. *Journal of Computational Physics*, 128(2):475–488, 1996.
15. D. A. Kopriva. *Implementing Spectral Methods for Partial Differential Equations*. Scientific Computation. Springer Netherlands, 2009.
16. D. A. Kopriva and G.J. Gassner. An energy stable discontinuous Galerkin spectral element discretization for variable coefficient advection problems. *SIAM Journal on Scientific Computing*, 36(4):A2076–A2099, 2014.
17. D. A. Kopriva, S. L. Woodruff, and M. Y. Hussaini. Computation of electromagnetic scattering with a non-conforming discontinuous spectral element method. *International Journal for Numerical Methods in Engineering*, 53(1):105–122, 2002.
18. J. E. Kozdon, E. M. Dunham, and J. Nordström. Simulation of dynamic earthquake ruptures in complex geometries using high-order finite difference methods. *Journal of Scientific Computing*, 55(1):92–124, 2013.
19. H.-O. Kreiss and G. Scherer. Finite element and finite difference methods for hyperbolic partial differential equations. In *Mathematical aspects of finite elements in partial differential equations; Proceedings of the Symposium*, pages 195–212, Madison, WI, 1974.
20. J. Nordström. Conservative finite difference formulations, variable coefficients, energy estimates and artificial dissipation. *Journal of Scientific Computing*, 29(3):375–404, 2006.
21. W. S. Slaughter. *The Linearized Theory of Elasticity*. Birkhäuser, 2002.
22. Timothy Warburton. A low storage curvilinear discontinuous Galerkin time-domain method for electromagnetics. In *Electromagnetic Theory (EMTS), 2010 URSI International Symposium on*, pages 996–999, August 2010.
23. Lucas C. Wilcox, Georg Stadler, Tan Bui-Thanh, and Omar Ghattas. Discretely exact derivatives for hyperbolic PDE-constrained optimization problems discretized by the discontinuous Galerkin method. *Journal of Scientific Computing*, 63(1):138–162, 2015.
24. Lucas C. Wilcox, Georg Stadler, Carsten Burstedde, and Omar Ghattas. A high-order discontinuous Galerkin method for wave propagation through coupled elastic-acoustic media. *Journal of Computational Physics*, 229(24):9373–9396, 2010.
25. T. A. Zang. On the rotation and skew-symmetric forms for incompressible flow simulations. *Applied Numerical Mathematics*, 7(1):27–40, 1991.